Quantum Mechanical Resolution Limits to Imaging and Spectroscopy in the Transmission Electron Microscope

S. J. Pennycook, [1] A. R. Lupini, [1] M. Varela, [1] A. Borisevich, [1] Y. Peng, [1] and P. D. Nellist [2]

[1] Oak Ridge National Laboratory, PO Box 2008 Oak Ridge TN 37830-6030 USA
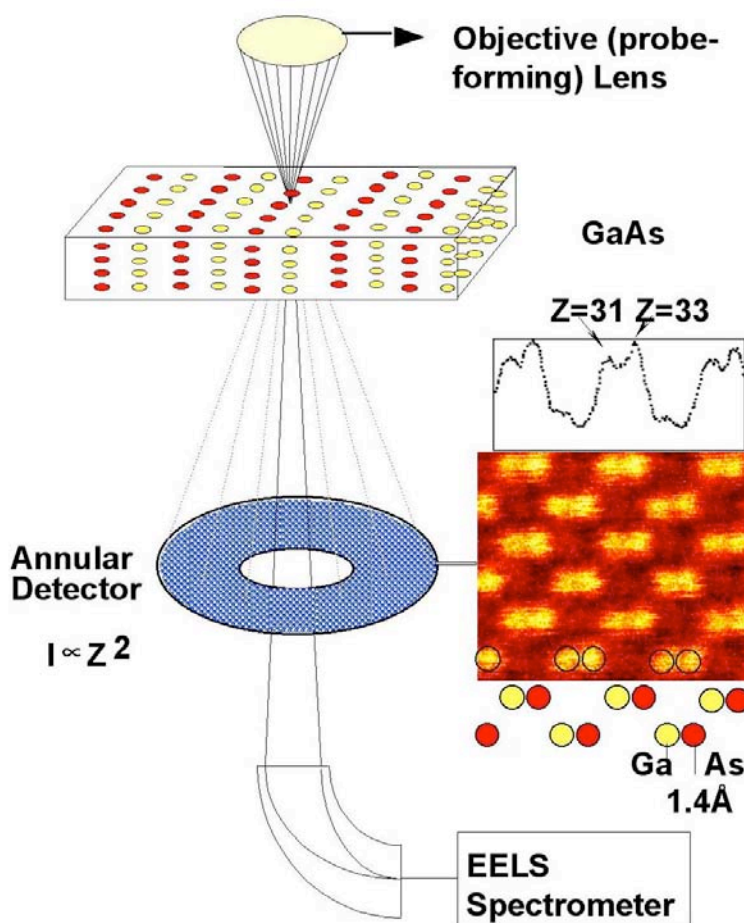[2] Nion Co., 1102 8th St., Kirkland, WA 98033, USA

1. Introduction

Until very recently, resolution in the electron microscope has been limited by the inherently large aberrations of the magnetic lenses used for image formation. Lens aberrations are very severe with magnetic lenses, limiting the resolution to $\sim 50 \lambda$ if uncorrected, whereas optical microscopes give resolutions $\sim \lambda$ through the use of wide apertures. In the last few years, however, advances in CCD detectors and increased computer power have allowed efficient diagnosis of aberrations and their successful correction using systems of multipole lenses (Dellby et al., 2001; Haider et al., 1998a; Haider et al., 1998b; Krivanek et al., 1999). Resolution has more than doubled in this time, and we are approaching a new era when electron microscopes will no longer be limited by their optics, and the fundamental quantum mechanical limit to resolution will soon be reached.

Here we present some of the recent results from the aberration-corrected microscopes at Oak Ridge National Laboratory (ORNL) showing the improvement in resolution and sensitivity to single atoms. Next we review the physics of imaging and spectroscopy from the perspective of the scanning transmission electron microscope (STEM), which allows a convenient comparison of the most common forms of imaging: bright field phase contrast imaging, as usually employed in the conventional high resolution electron microscope, incoherent Z-contrast microscopy using an annular dark field (ADF) detector, and energy-filtered imaging or spectroscopy. As shown in the schematic of Fig. 1, electrons passing through the central hole in the annular detector can be collected *simultaneously* with the ADF image, allowing direct comparison with bright field images, or electron energy loss spectroscopy to be carried out at atomic resolution, using the ADF image to precisely locate the probe over a specific atomic column or plane (Batson, 1993; Browning et al., 1993; Dickey et al., 1997; Duscher et al., 1998; Wallis et al., 1997).

Different detectors give entirely different views of the specimen, showing completely different contrast, resolution limits, and sensitivity to individual atoms. This is true even though the intensity of the scanning probe is identical in each case. It is often tempting to be a "super-observer", and to make interpretations independent of the detector configuration. We will develop a quantum-mechanical perspective, that the entire system of incident beam, specimen and detector represents one quantum mechanical measurement system, and that the view of the specimen does depend on how you look at it (Pennycook, 2002).

Fig. 1. Schematic showing simultaneous Z-contrast imaging and EELS in the STEM. A probe of atomic dimensions is scanned across a thin TEM specimen, and an image is formed by mapping the variation in some scattered electron flux. The annular detector integrates scattering over a wide range of relatively high angles. This gives a Z-contrast image reflecting total scattered intensity reaching the detector. For sufficiently high inner angle this is approximately proportional to Z^2, where Z is atomic number, as demonstrated by the image of GaAs, in which the sublattice polarity is distinguished. Simultaneously, the transmitted beam may be detected to form a bright field image, or it may be filtered by a spectrometer to give elemental specific images or an electron energy loss spectrum. This is formally equivalent to X-ray absorption spectroscopy, but in the STEM is obtained at atomic resolution.

2. Recent Examples of Aberration Correction at ORNL

Both the VG Microscopes' STEMs at Oak Ridge National Laboratory (ORNL) are now fitted with aberration correctors constructed by Nion Co. The 100 kV HB501UX has seen its resolution from improved 2.2 Å (full-width-half-maximum probe intensity) to around 1.1 Å. It is now comparable in performance to the *uncorrected* 300 kV HB603U STEM at ORNL which, before correction, had a directly interpretable resolution of 1.3 Å. Figure 2 shows the approximately 2.5 times greater angular range available to form the probe, and the resulting ~ 2 times improved resolution in a Si ⟨110⟩ crystal, where the dumbbell spacing of 1.36 Å is now clearly resolved (Lupini and Pennycook, 2003). Figure 3 shows the sensitivity to single atoms available with the enhanced resolution, where single Bi atoms on lattice sites within the crystal are visible. Similar results have been shown also for Sb atoms in Si using an uncorrected 200 kV microscope (Voyles et al., 2002). In our case, intensity profiles across the image reveal which of the two columns of the dumbbell contain the Bi atom. The density of bright spots correlates with the known dose of Bi, which was introduced by ion implantation followed by recrystallization through solid phase epitaxial growth.

Fig. 2. Ronchigram observed in far-field with a probe stationary on the sample showing the extent of uniform phase (a) for the uncorrected microscope (b) after aberration correction. Images of Si ⟨110⟩ show the improvement in image resolution from (c) 2.2 Å to (d) 1.3 Å which now resolves the dumbbells.
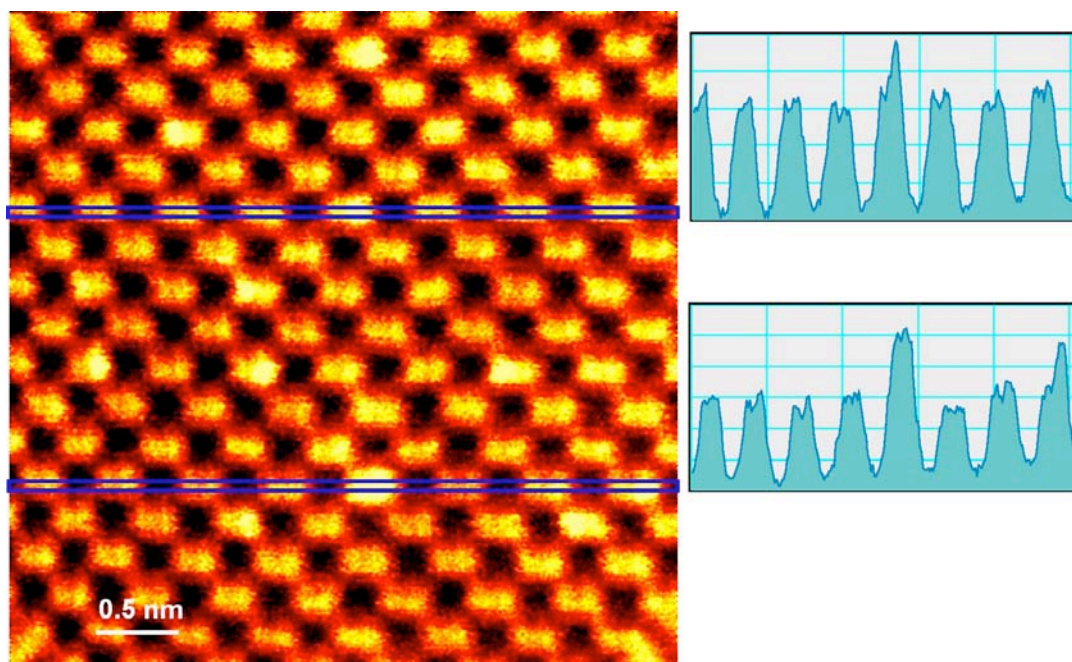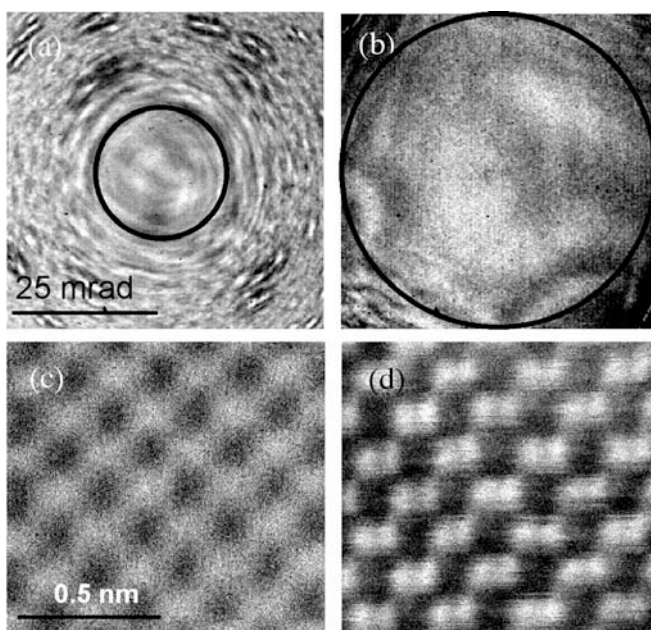

Fig. 3. Z-contrast image of Bi-doped Si ⟨110⟩ revealing the columns containing individual Bi atoms. The upper intensity profile shows a Bi atom on the right hand column of a Si dumbbell, the lower profile shows a Bi atom in each of the two columns of a dumbbell.

The improved resolution of the 300 kV STEM is shown in Fig. 4, which compares images of single La atoms on a γ-alumina support before and after aberration correction. Although they are visible in both images, they show more contrast and a better signal to noise ratio after correction. A histogram of the full-width-half-maxima (FWHM) of intensity profiles across single La atoms (Fig. 4 (b), inset) gives the probe FWHM as about 0.7 – 0.8 Å. Line scans were taken in the vertical direction to avoid the effects of drift, which was predominantly in the horizontal direction. The smaller probe also gives a greatly improved image from the alumina itself. Although

very faint lattice fringes can be discerned in the uncorrected image (arrowed), after correction, individual Al/O columns are clearly seen in Fig. 4 (c). The La atom positions are directly seen to coincide with (100) atomic columns of the spinel lattice of γ-Al$_2$O$_3$.
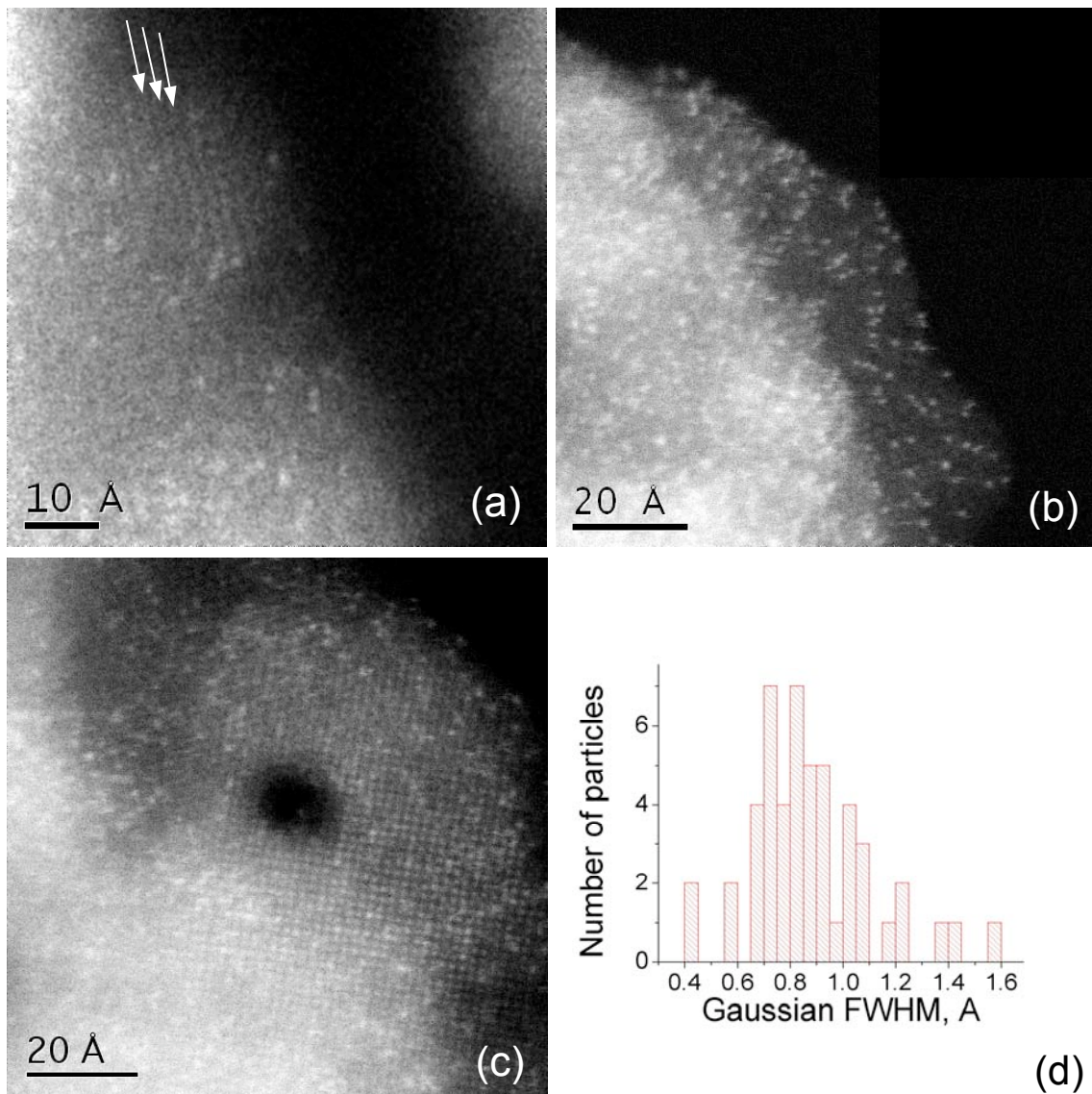

Fig. 4. Images of La-doped γ-alumina obtained with a 300 kV STEM before (a) and after (b, c) aberration correction, showing the improvement in contrast, resolution and signal to noise ratio. In (b) single La atoms are seen on a randomly oriented substrate, with (d) a histogram of the FWHM from intensity profiles. In (c) La atoms are visible at the same time as a γ-Al$_2$O$_3$ lattice viewed in the [100] direction.

An ideal demonstration of the ability of the STEM to probe highly localized changes in electronic structure is provided by the high T$_c$ superconductor YBCO. In this layered structure, superconductivity is believed to occur as a result of charge transfer from the CuO chain plane, where the Cu valence is nominally +1, to the CuO$_2$ plane

where the Cu valence is nominally +2. The Cu $L_{2,3}$ white line ratio should therefore change on moving the probe from the chains to the planes, a distance of only ~ 4 Å. As seen in Fig 5, this is exactly what is observed experimentally. Furthermore, it has been well-established that a pre-peak observed on the O K edge is directly related to the density of holes responsible for superconductivity (Browning et al., 1992). Fig. 5 also shows that this pre-peak appears present in the planes but not in the chains, suggesting hole localization in the CuO_2 planes. Further studies are required to ensure that damage effects are not playing a role, but this is an excellent demonstration of the local nature of the information in the EELS spectrum. Because of dynamical scattering, the probe explores neighboring columns as it propagates through the specimen, but the information seen by a large angle EELS detector is still highly localized, almost as highly localized as with the high angle annular dark field detector itself. (Lupini and Pennycook, 2003)
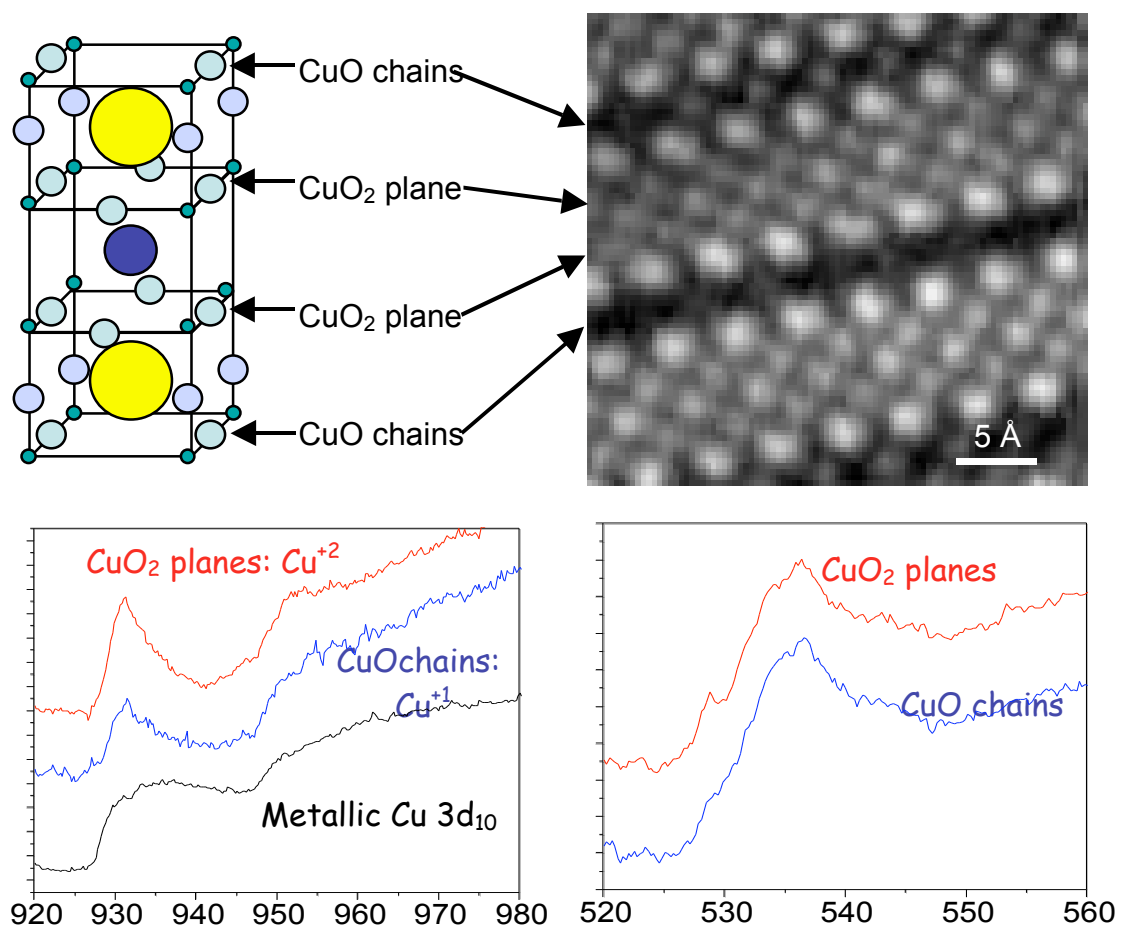

Fig. 5. Schematic of YBCO structure with Cu/O planes and chains arrowed in the Z-contrast image. Spectra obtained from the chains and planes separately show (left) their different $L_{2,3}$ ratio at the Cu edge, with metallic Cu as a reference, and (right) a prepeak in the O K edge region of the spectra indicating holes localized in the planes.

3. Quantum Mechanical Aspects of Electron Microscopy

Figure 6 shows a ray diagram that is commonly used to describe image formation in the STEM. The electron source, ideally a cold field emission gun, is arranged to illuminate the back focal plane of the objective lens with a coherent wave front. Then a focused, coherent probe can be formed at the specimen. Previously this was done using simple round condenser lenses to demagnify the source and form a coherent patch as shown in Fig. 2a. Now the illumination involves more complicated optics, but the goal remains to form a coherent wave front in the back focal plane, albeit larger, and with the appropriate aberrations to compensate for the intrinsic aberrations of the objective lens. With a crystalline sample, diffraction causes periodic replication of the objective aperture. Contrast is caused by the overlap of these discs and the interference of different ray paths as the probe is scanned. Image contrast at spatial frequency ρ has a contribution from interference of the two incident paths shown, separated by ρ which scatter to the same region of the annular detector. Electrons that are scattered outside the range of overlapping discs do not have a choice of paths. Just like the case of Young's fringes from a pair of slits, interference is not seen if one slit is covered up. Electrons outside the overlap regions carry no image information.
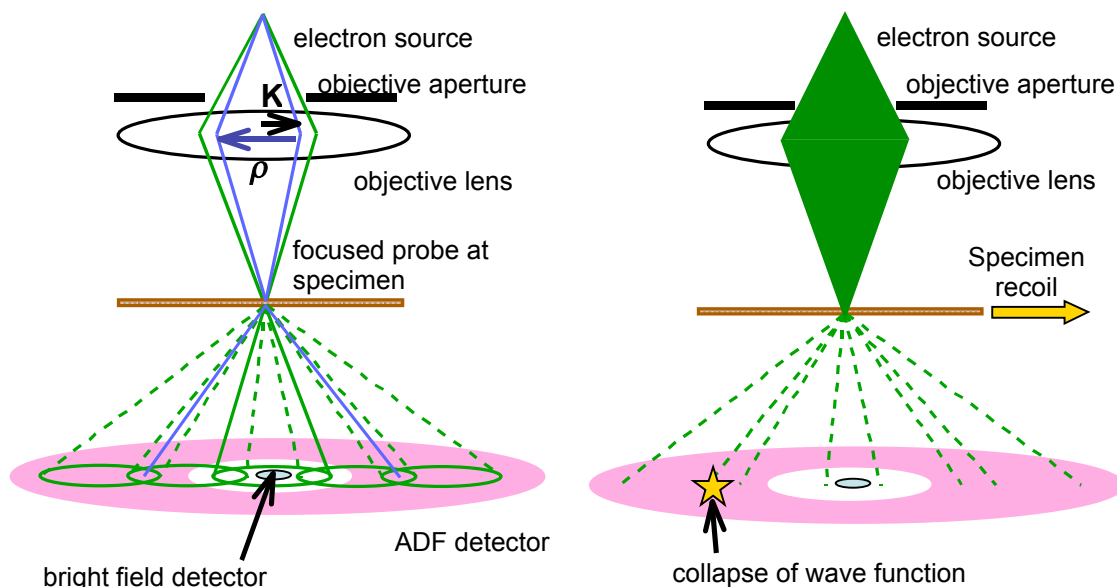

Fig. 6. Schematic of image formation in the STEM, left, in a wave optics viewpoint, right, in a particle viewpoint..

The diagram also shows a small axial detector. Electrons that pass through this aperture produce a bright field image as the probe is scanned, equivalent by reciprocity to the phase contrast images of a conventional TEM. Reciprocity is based on the principle of time-reversal symmetry and the fact that most contrast arises through elastic scattering. Thus, images obtained with this detector in the STEM are equivalent to those obtained using the same apertures in TEM, with the electrons traveling from bottom to top in the figure. The image is formed in parallel in the TEM, but is optically identical. For the crystal spacings represented in the figure, no bright field lattice fringes exist, since no overlaps fall on the axial detector. This is

the origin of the enhanced resolution of ADF STEM compared to bright field imaging. Spacings can be resolved up to the spatial frequency ρ which corresponds to the objective aperture diameter, whereas bright field imaging cuts off at the spatial frequency $\mathbf{K}$, corresponding to the aperture radius, a factor of two smaller.

A particle viewpoint of the process also makes clear the central role of the detector. In a particle picture a single electron is prepared in the form of a converging spherical wave and propagates through the specimen. The diffraction pattern represents the probability that the electron strikes a certain position on the screen or detector. Even the single electron explores all possible pathways and undergoes the entire interference process of diffraction, even though the wave function finally collapses to a point when it reaches the detector. That point, however, is only determined when the electron hits the screen, not when the electron leaves the specimen. Only when the wave function collapses is the direction of recoil determined, which for microscope dimensions ~ 1m and electron velocities ~ 10^8 m/s is ~ 10 ns after it passed through the specimen. The electron microscope is a fine example of the non-local nature of quantum mechanics, and highlights the fact that we must consider the entire system of specimen and detector as one quantum mechanical measurement system

It should not be surprising, therefore, that the image of the sample depends on how we look at it. Figure 7 shows one of the earliest illustrations of this point. It compares bright field and ADF images of a Si crystal, recorded simultaneously using the 100 kV STEM. One key difference in the nature of the images is immediately obvious. The bright field images show strong interference effects, in this case thickness fringes, whereas the ADF image shows no such fringes and appears to be incoherent in nature.
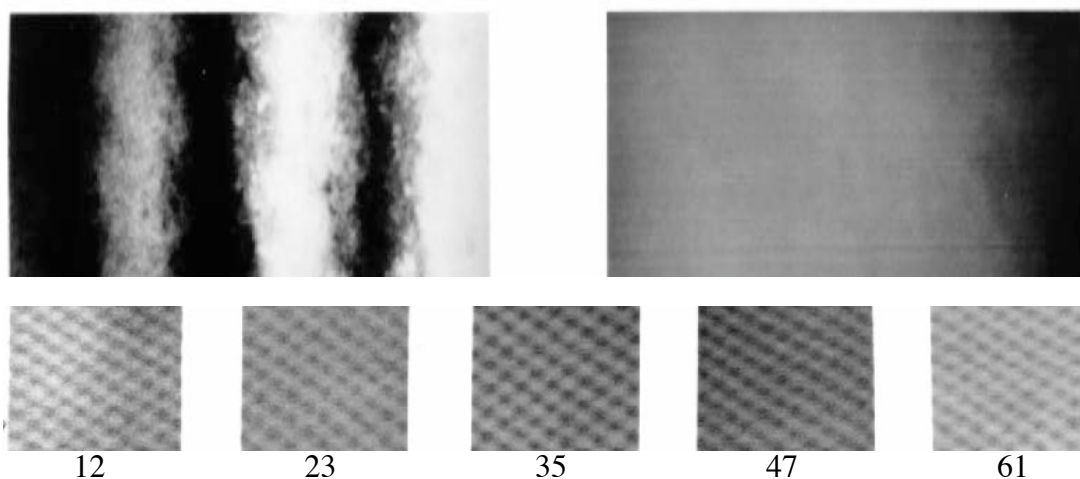

| 12 | 23 | 35 | 47 | 61 |

Fig. 7. Illustration of simultaneous coherent and incoherent imaging on the STEM using a small bright field detector and a large annular detector, respectively. The images of a Si crystal in <110> orientation show very different characteristics; the bright field detector shows thickness fringes indicative of a coherent image (left), whereas the annular detector (right) shows an atomic resolution structure image similar in form at all thicknesses (given in nm) suggestive of an incoherent image. Images recorded using a VG Microscopes HB501UX STEM at 100 kV with a probe size of ~ 0.22 nm.

Much effort has been expended over the last 15 years in trying to understand the reason the ADF images show incoherent characteristics, even from thick crystals in which the probe has undergone multiple scattering. Again, this also can only be understood in a quantum mechanical framework. While there are many calculations of image contrast that are consistent with the view of the ADF image as an incoherent image, as long as the central hole is sufficiently large (Anderson et al., 1997; Hartel et al., 1996; Ishizuka, 2001; Loane et al., 1992; Mitsuishi et al., 2001; Nakamura et al., 1997), image simulations do not reveal the underlying physical explanation for such behavior; a Bloch wave analysis reveals that the high angle detector acts as a quantum filter, allowing only highly localized Bloch states to contribute to the image (Nellist and Pennycook, 2000; Pennycook and Jesson, 1990; Pennycook and Jesson, 1991; Pennycook and Nellist, 1999). For the fast electron propagating along the zone axis of a crystal, the Bloch states are cylindrical states showing the symmetry of the projected unit cell (Bird, 1989). As with atomic orbitals, the 1s state represents the most strongly bound state, and is the most localized about the atomic column. It is therefore the broadest state in reciprocal space and so dominates the intensity at sufficiently high angles.

Coherent Imaging, Incoherent Imaging and Localization.

Figure 8 shows a very recent example from the aberration-corrected 300 kV STEM, the imaging of individual La atoms on a thin piece of γ-alumina. The single atoms show very clearly on the ADF image, whereas they are invisible on the bright field image which is dominated by coherent interference effects from the support. The ADF image also shows only one focus, characteristic of an incoherent image, whereas the BF image shows contrast reversals typical of coherent imaging, but never reveals the individual La atoms. Partly this is indicative of the Z-contrast seen for high angle elastic scattering to the annular detector, but it also reflects the reduced coherence volume associated with incoherent imaging. There is simply less specimen contributing to the image from any given point.
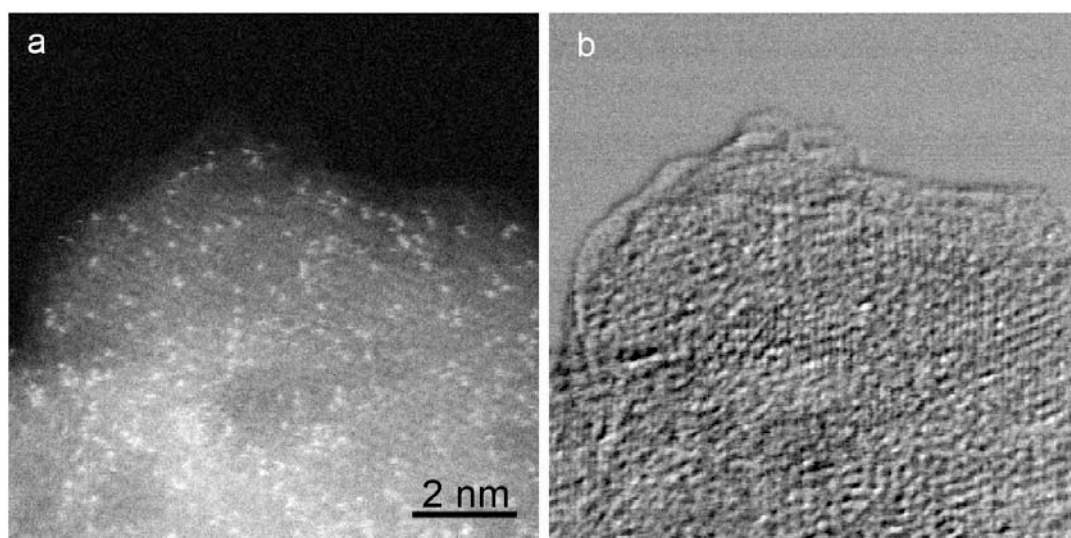

Fig. 8. Comparison of (a) HAADF image and (b) bright field image of La stabilized γ-alumina obtained simultaneously on the aberration-corrected 300 kV STEM.

The difference is quite fundamental to the different modes of imaging. Lord Rayleigh first described the difference between coherent and incoherent imaging in the context of the light microscope (Rayleigh, 1896). Incoherent imaging applies when there are no phase relations between the light emitting from different points on the object, as for a self-luminous object. However, for non-luminous objects Lord Rayleigh showed that effective incoherent imaging could be achieved with a convergent source of illumination provided by a condenser lens. The *large* convergence angle gives a *short* transverse coherence length in the specimen, effectively breaking the coherence between neighboring points and giving a very good approximation to ideal incoherent imaging.

The annular detector on the STEM gives the equivalent effect for electrons, as shown schematically in Fig. 9. Coherent or incoherent imaging now depends on the transverse coherence length L_t seen from the detector compared to the atomic spacing d. For L_t much smaller than an atomic spacing, coherent imaging results. Conversely, if L_t is much larger than an atomic spacing, neighboring columns are effectively imaged independently and incoherent imaging results.
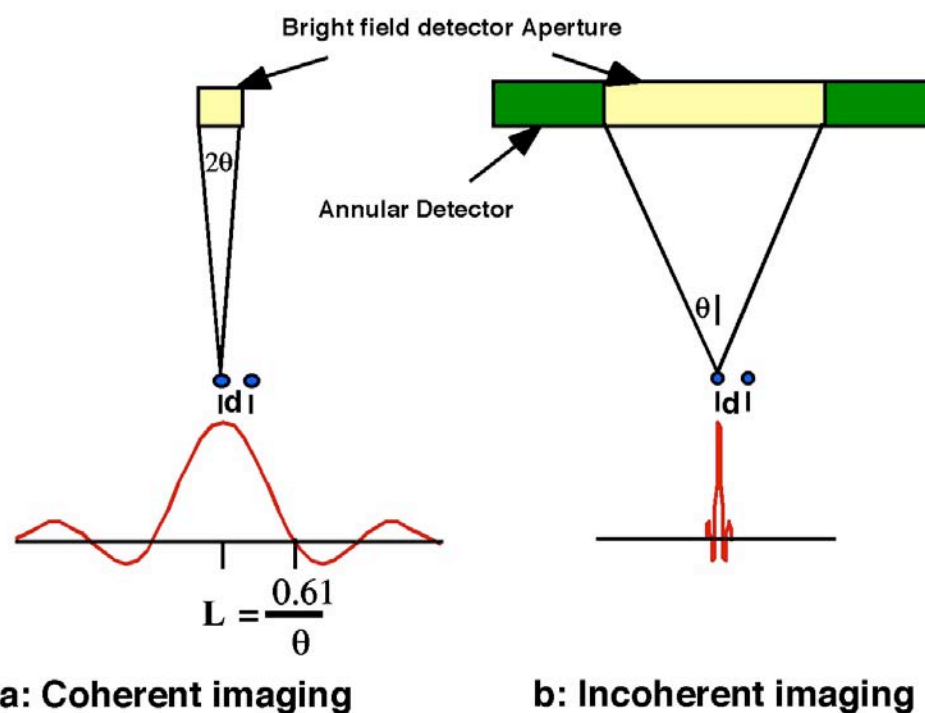

Fig. 9. Schematic showing how the transverse coherence length L seen by the detector aperture (illumination aperture in TEM) determines if neighboring atoms are imaged coherently (a) or incoherently (b). Incoherent imaging applies not only to the annular detector but also to a wide angle axial detector, as often used for EELS.

One can also view the action of the detector as a Bloch state filter to be a consequence of the coherence envelope imposed on the Bloch states: for a small coherence envelope, only the most localized states are important and the remainder are ineffective. Another consequence of the short transverse coherence length is that thermal vibrations become more significant. As the inner detector angle is increased, the transverse coherence length becomes comparable to thermal vibration amplitudes,

and the detected intensity becomes dominated by diffuse scattering. This effectively breaks the coherence through the sample thickness, giving an effective thickness integration of scattered intensity. Recently, direct images of thermal vibration anomalies in a solid have been obtained using ADF STEM (Abe et al., 2003).

Another important difference between coherent and incoherent imaging is the lack of a phase problem with the latter. Consider a wave function $\psi(\mathbf{R})$ on the specimen exit surface. In coherent imaging, the wave function *amplitude* is convolved with an *amplitude* point spread function, giving an image intensity of

$$I(\mathbf{R}) = \left| \psi(\mathbf{R}) * P(\mathbf{R}) \right|^2. \tag{1}$$

This has a phase problem in that atoms can appear black or white. In an incoherent image, I($\mathbf{R}$) is described as a convolution of *intensities*,

$$I(\mathbf{R}) = \left| \psi(\mathbf{R}) \right|^2 * \left| P(\mathbf{R}) \right|^2, \tag{2}$$

which has no phase problem. Furthermore, the effective point spread function is sharper than for coherent imaging, reflecting again the increased resolution available with incoherent imaging.

It would appear from the above discussion of coherence lengths that incoherent imaging is *intrinsically* more localized than coherent imaging, in which, by definition each image point must involve contributions from regions remote from that point. As a specific illustration of the role of the detector, we can rewrite eqn. 1. as an explicit integral over a detector described by the detector function D($\mathbf{K}$), which is unity of the range of scattering angles accepted by the detector and zero elsewhere. For a probe coordinate $\mathbf{R}_0$, $\psi(\mathbf{R},\mathbf{R}_0)$ is the exit face wave function, its Fourier transform $\psi(\mathbf{K},\mathbf{R}_0)$ is the amplitude in the detector plane, and the image intensity for point $\mathbf{R}_0$ is given by integrating the intensity over the detector, (Lupini and Pennycook, 2003)

$$I(\mathbf{R}_0) = \int D(\mathbf{K}) \Psi(\mathbf{K},\mathbf{R}_0) \Psi^*(\mathbf{K},\mathbf{R}_0) d\mathbf{K} \tag{3}$$

Since the detector function is real and only takes values 0 and 1, we can use Parseval's theorem to rewrite the integral in real space as

$$I(\mathbf{R}_0) = \int \left| \int \psi(\mathbf{R}',\mathbf{R}_0) d(\mathbf{R} - \mathbf{R}',\mathbf{R}_0) d\mathbf{R}' \right|^2 d\mathbf{R} \tag{4}$$

where d($\mathbf{R}$) is the Fourier transform of the detector function D($\mathbf{K}$). This form makes clear that the real space distribution of intensity *as seen by the detector* from a probe at $\mathbf{R}_0$ is just the integrand in Eqn. 4,

$$I'(\mathbf{R},\mathbf{R}_0) = \left| \int \psi(\mathbf{R}',\mathbf{R}_0) d(\mathbf{R} - \mathbf{R}',\mathbf{R}_0) d\mathbf{R}' \right|^2, \tag{5}$$

which is the intensity following a *convolution* of the exit face wave function with the real space detector function. For coherent bright field imaging the detector is small, and therefore $d(\mathbf{R})$ is broad in real space, and therefore any fine details in the exit face wave function will be lost by the convolution. The larger the angular range of the

detector, the narrower is $d(\mathbf{R})$, and the fine details are preserved. Thus we see again that coherent imaging is intrinsically delocalized. Examples of the intensity distributions $I'(\mathbf{R},\mathbf{R}_0)$ for different detectors for a 100 kV probe located over one column of a dumbbell in Si [110] are shown in Fig. 10. As the bright field detector angle is increased, localization increases markedly. This is directly relevant to the localization of EELS data, and shows how large acceptance angles are necessary for column-by-column spectroscopy. The complementary ADF detector is more localized still, because of the absence of the low angles, and also becomes further localized as the inner detector angle is increased. The small bright point in the center of the ADF detector distributions represents the 1s Bloch state on the Si column, consistent with the Bloch wave analysis that the 1s state is the primary contribution to image contrast. The faint, less localized features come from less localized states. These states give negligible contrast but do contribute to the background in the image.
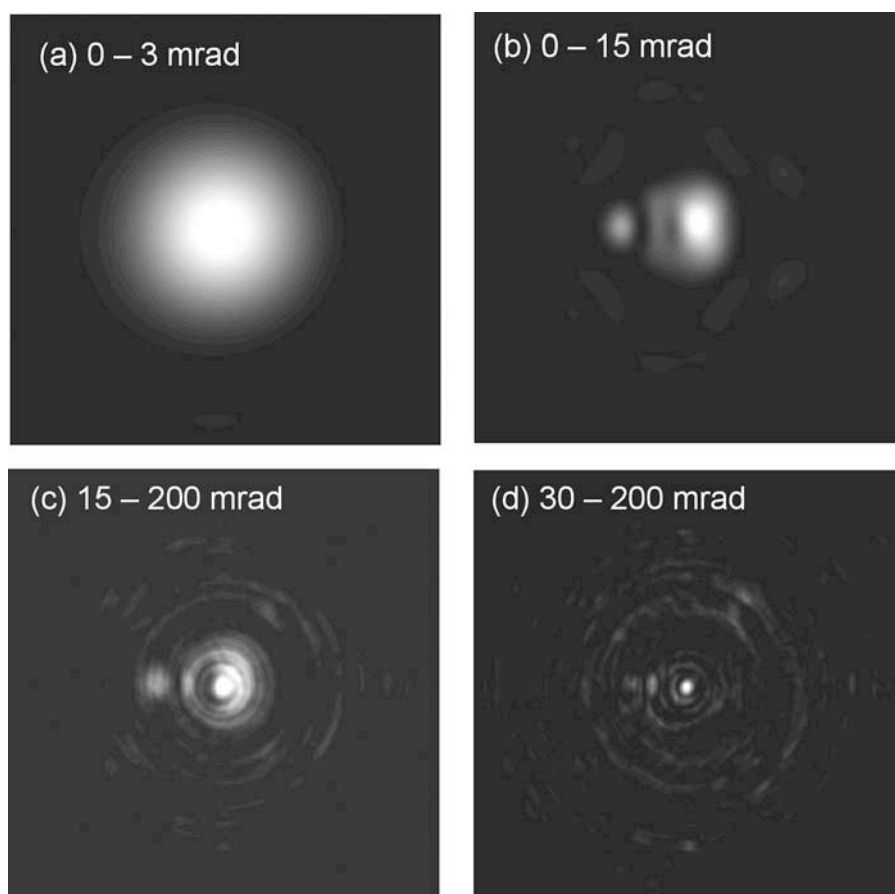

Fig. 10. Spatial distribution of detected intensity for a probe located over one column in Si [110] as seen by various detectors. Specimen thickness 76.8 Å, field of view 7.5 x 7.5 Å, probe parameters, C_s = 0.5 mm, defocus – 43 nm, semiangle 13.3 mrad. Calculated by a multislice code (Kirkland, 1998) with 10 phonon configurations at 300 K.

4. Future Directions

The increased resolution, contrast and signal to noise ratio made possible through aberration correction is clear from the examples given above. Plans exist to correct even higher order aberrations (Dellby et al., 2001), allowing even finer probes to be formed as shown in Fig. 11.
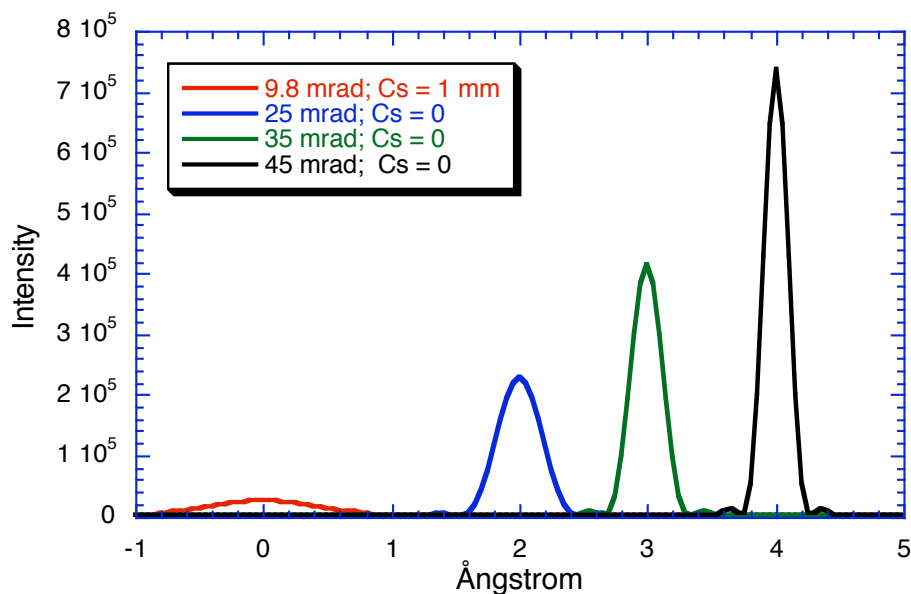

Fig. 11. Probe intensity profiles for a 300 kV STEM with spherical aberration under optimum defocus of − 45 nm, and for various apertures after aberration correction, normalized to the same total incident intensity through the aperture.

Although chromatic aberration becomes increasingly important, transferring intensity from the central peak into the tails of the probe, the question arises as to the fundamental resolution limit. For a single atom, the resolution limit would be just the high angle components of the atomic potential, thermally smeared, and the resolution limit would be the mean square thermal vibration amplitude. Based on the Bloch wave analysis, it was proposed that the fundamental limit in a zone axis crystal, in the presence of multiple elastic scattering, would be the 1s state (Pennycook et al., 2000). This is borne out by calculations for an aberration free probe of 0.57 Å FWHM, as shown in Fig 12.

Fig. 12. Intensity of the (a) As and (b) Ga 1s states in [110] GaAs for a 300 kV electron beam, compared to ADF image intensity contributions at a thickness of (c) 10 Å and (d) 1000 Å, showing that the image resembles a direct image of the 1s states. Calculated for a detector angle of 45 - 96 mrad, 849 reflections and 165 incident beams, not including absorption.

(a) As 1s

(b) Ga 1s

(c) Image, t = 10 Å
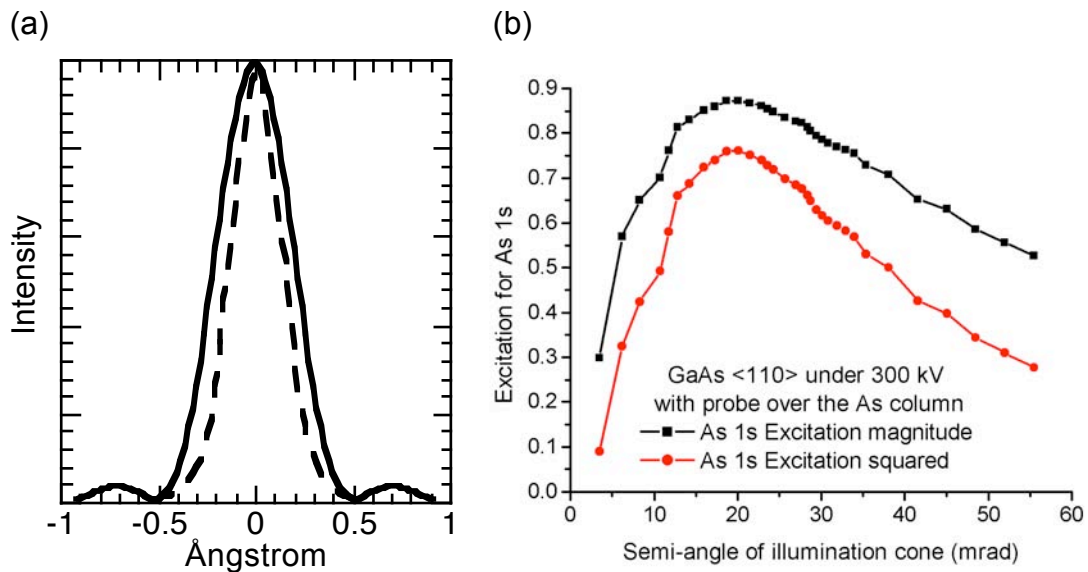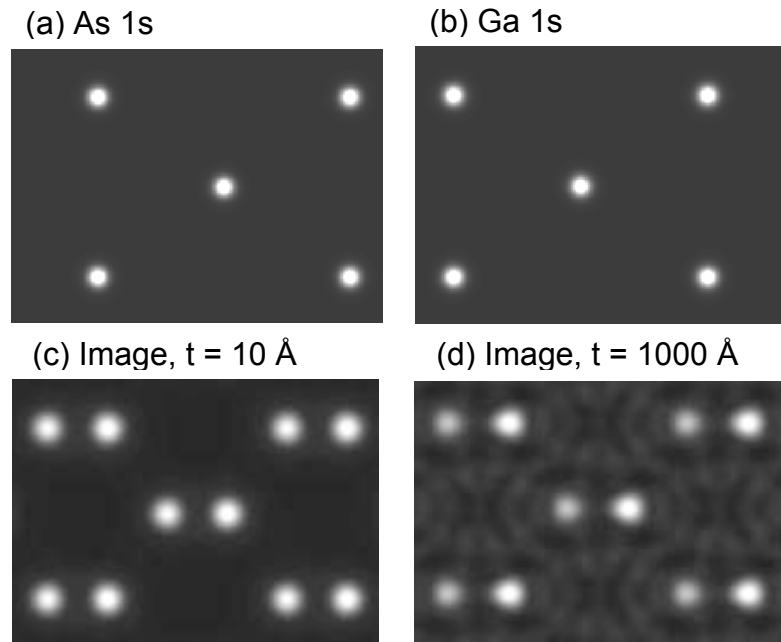
(d) Image, t = 1000 Å

(a)

(b)

Fig. 13. (a) Intensity profile of the 300 kV aberration free probe (solid line) formed with an aperture semiangle of 23 mrad compared to the As 1s state intensity (dashed line). (b) Angular dependence of the coupling between the incident probe and the As 1s state showing that the optimum angle for maximum 1s state excitation is close to 23 mrad.

In fact under these conditions the probe itself is very similar to the 1s states, as shown in Fig. 13(a). If a particle is prepared in an eigenstate of a filter device, then it will be directly transmitted. The aberration corrected probe closely matches the 1s states, and therefore, if it enters the crystal over a column of atoms, it will go straight down the column, scattering to the ADF detector as it propagates. If the probe enters between the column, there is no 1s state to couple into, and the probe decomposes large number of less localized states which do not scatter efficiently into the ADF detector. Thus it is entirely reasonable that the image represents a direct image of the

1s states. The angular dependence of the overlap between the probe and the As 1s state is shown in Fig. 13(b) and has a maximum at an angle of ~ 20 mrad.

This raises the question of what the image might look like at even larger aperture angles. It is possible that aberration correction may open up modes of microscopy that were never before possible. Confocal imaging has revolutionized optical microscopy by facilitating 3D tomography through depth sectioning. ADF STEM is ideal for tomography since the images show no contrast reversals with focus, which is a key requirement. If the probe-forming aperture is doubled again, to 50 mrad or above, then most of the probe intensity is contained in the high angle components of the probe. These are traveling at a sufficiently high angle to the crystal zone axis that they will propagate as plane waves, not exciting the Bloch states at all. Such beams are scattered *only kinematically* by the sample, and will therefore come to a focus at a unique depth in the specimen. Depth sectioning will become a viable technique in electron microscopy for the first time, as depicted schematically in Fig. 15. Thus with a small aperture the crystal lattice could be imaged in projection, while 3D tomography could be achieved with a larger aperture. Furthermore, EELS data or X-ray fluorescence data could also be collected and reconstructed in 3D, providing the ultimate analysis: 3D reconstruction at atomic resolution with single atom identification.
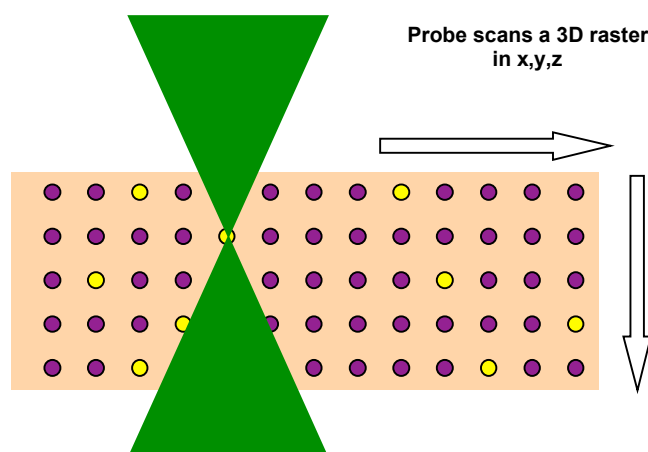

Fig. 15. Schematic showing depth sectioning in the STEM. The impurity atoms (lighter) may be identified from the image or by spectroscopy and the entire specimen reconstructed at atomic resolution in 3D.

5. Summary

The correction of aberrations in the electron microscope removes the major barrier to resolution that has existed since its invention. The greatly improved sensitivity and signal to noise ratio is expected to allow single atom sensitivity not only in imaging but also in spectroscopy, perhaps even in three dimensions. The ultimate sensitivity will become available for determining trap states in optical and electronic devices, the active sites and mechanisms in catalysis, the origin of strength and ductility in structural materials and the functionality of individual nanostructures.

6. Acknowledgements

7. References

Abe, E., Pennycook, S. J., and Tsai, A. P. (2003). Direct observation of a local thermal vibration anomaly in a quasicrystal. *Nature* **421,** 347-350.

Anderson, S. C., Birkeland, C. R., Anstis, G. R., and Cockayne, D. J. H. (1997). An approach to quantitative compositional profiling at near-atomic resolution using high-angle annular dark field imaging. *Ultramicroscopy* **69,** 83-103.

Batson, P. E. (1993). Simultaneous STEM imaging and electron energy-loss spectroscopy with atomic column sensitivity. *Nature* **366**.

Bird, D. M. (1989). Theory of Zone Axis Electron-Diffraction. *Journal of Electron Microscopy Technique* **13,** 77-97.

Browning, N. D., Chisholm, M. F., and Pennycook, S. J. (1993). Atomic-Resolution Chemical-Analysis Using a Scanning-Transmission Electron-Microscope. *Nature* **366,** 143-146.

Browning, N. D., Yuan, J., and Brown, L. M. (1992). Determination of the Local Oxygen Stoichiometry in $YBa_2Cu_3O_{7-\delta}$ by Electron-Energy Loss Spectroscopy in the Scanning-Transmission Electron-Microscope. *Physica C* **202,** 12-18.

Dellby, N., Krivanek, O. L., Nellist, P. D., Batson, P. E., and Lupini, A. R. (2001). Progress in aberration-corrected scanning transmission electron microscopy. *Journal of Electron Microscopy* **50,** 177-185.

Dickey, E. C., Dravid, V. P., Nellist, P. D., Wallis, D. J., Pennycook, S. J., and Revcolevschi, A. (1997). Structure and bonding at Ni-ZrO_2 (cubic) interfaces formed by the reduction of a NiO-ZrO_2 (cubic) composite. *Microscopy and Microanalysis* **3,** 443-450.

Duscher, G., Browning, N. D., and Pennycook, S. J. (1998). Atomic column resolved electron energy-loss spectroscopy. *Physica Status Solidi a-Applied Research* **166,** 327-342.

Haider, M., Rose, H., Uhlemann, S., Schwan, E., Kabius, B., and Urban, K. (1998a). A spherical-aberration-corrected 200 kV transmission electron microscope. *Ultramicroscopy* **75,** 53-60.

Haider, M., Uhlemann, S., Schwan, E., Rose, H., Kabius, B., and Urban, K. (1998b). Electron microscopy image enhanced. *Nature* **392,** 768-769.

Hartel, P., Rose, H., and Dinges, C. (1996). Conditions and reasons for incoherent imaging in STEM. *Ultramicroscopy* **63,** 93-114.

Ishizuka, K. (2001). Prospects of atomic resolution imaging with an aberration-corrected STEM. *Journal of Electron Microscopy* **50,** 291-305.

Kirkland, E. J. (1998). "Advanced Computing in Electron Microscopy." Plenum Press, New York.

Krivanek, O. L., Dellby, N., and Lupini, A. R. (1999). Towards sub-angstrom electron beams. *Ultramicroscopy* **78,** 1-11.

Loane, R. F., Xu, P., and Silcox, J. (1992). Incoherent Imaging of Zone Axis Crystals with ADF STEM. *Ultramicroscopy* **40,** 121-138.

Lupini, A. R., and Pennycook, S. J. (2003). Localization in Elastic and Inelastic Scattering. *Ultramicroscopy,* (in press).

Mitsuishi, K., Takeguchi, M., Yasuda, H., and Furuya, K. (2001). New scheme for calculation of annular dark-field STEM image including both elastically diffracted and TDS waves. *Journal of Electron Microscopy* **50,** 157-162.

Nakamura, K., KaKibayashi, H., Kanehori, K., and Tanaka, N. (1997). Position dependence of the visibility of a single gold atom in silicon crystals in HAADF-STEM image simulation. *Journal of Electron Microscopy* **46,** 33-43.

Nellist, P. D., and Pennycook, S. J. (2000). The principles and interpretation of annular dark-field Z-contrast imaging. *Advances in Imaging and Electron Physics* **113,** 147-203.

Pennycook, S. J. (2002). Structure determination through Z-contrast microscopy. *In* "Advances in Imaging and Electron Physics, Vol 123." (P. G. Merli, G. Calestani, and M. Vittori-Antisari, Eds.), pp. 173-206. Advances in Imaging and Electron Physics.

Pennycook, S. J., and Jesson, D. E. (1990). High-Resolution Incoherent Imaging of Crystals. *Physical Review Letters* **64,** 938-941.

Pennycook, S. J., and Jesson, D. E. (1991). High-Resolution Z-Contrast Imaging of Crystals. *Ultramicroscopy* **37,** 14-38.

Pennycook, S. J., and Nellist, P. D. (1999). Z-Contrast Scanning Transmission Electron Microscopy. *In* "Impact of Electron and Scanning Probe Microscopy on Materials Research." (D. G. Rickerby, U. Valdré, and G. Valdré, Eds.), pp. 161-207. Kluwer Academic Publishers.

Pennycook, S. J., Rafferty, B., and Nellist, P. D. (2000). Z-contrast imaging in an aberration-corrected scanning transmission electron microscope. *Microscopy and Microanalysis* **6,** 343-352.

Rayleigh, Lord. (1896). On the theory of optical images with special reference to the microscope. *Philosophical Magazine (5)* **42,** 167–195.

Voyles, P. M., Muller, D. A., Grazul, J. L., Citrin, P. H., and Gossmann, H. J. L. (2002). Atomic-scale imaging of individual dopant atoms and clusters in highly n-type bulk Si. *Nature* **416,** 826-829.

Wallis, D. J., Browning, N. D., Sivananthan, S., Nellist, P. D., and Pennycook, S. J. (1997). Atomic layer graphoepitaxy for single crystal heterostructures. *Applied Physics Letters* **70,** 3113-3115.